bioRxiv preprint doi: https://doi.org/10.1101/069559; this version posted August 16, 2016. The copyright holder for this preprint (which was not certified by peer review) is the author/funder. All rights reserved. No reuse allowed without permission.

# Molecular mechanisms of substrate-controlled ring dynamics and sub-stepping in a nucleic-acid dependent hexameric motor

Nathan D. Thomsen[1,2], Michael R. Lawson[1], Lea B. Witkowsky[1], Song Qu[1,3], and James M. Berger[1,4*]

[1]Department of Molecular and Cell Biology and QB3 Institute, University of California, Berkeley CA 94720. Present address: [2]Gilead Sciences Inc, Foster City, CA. [3]Scripps Research Institute, La Jolla, CA. [4]Department of Biophysics and Biophysical Chemistry, Johns Hopkins School of Medicine, Baltimore, MD.

*To whom correspondence should be addressed: jmberger@jhmi.edu

bioRxiv preprint doi: https://doi.org/10.1101/069559; this version posted August 16, 2016. The copyright holder for this preprint (which was not certified by peer review) is the author/funder. All rights reserved. No reuse allowed without permission.

## ABSTRACT

Ring-shaped hexameric helicases and translocases support essential DNA, RNA, and protein-dependent transactions in all cells and many viruses. How such systems coordinate ATPase activity between multiple subunits to power conformational changes that drive the engagement and movement of client substrates is a fundamental question. Using the *E. coli* Rho transcription termination factor as a model system, we have employed solution and crystallographic structural methods to delineate the range of conformational changes that accompany distinct substrate and nucleotide cofactor binding events. SAXS data show that Rho preferentially adopts an open-ring state in solution, and that RNA and ATP are both required to cooperatively promote ring closure. Multiple closed-ring structures with different RNA substrates and nucleotide occupancies capture distinct catalytic intermediates accessed during translocation. Our data reveal how RNA-induced ring closure templates a sequential ATP-hydrolysis mechanism, provide a molecular rationale for how the Rho ATPase domains distinguishes between distinct RNA sequences, and establish the first structural snapshots of substepping events in a hexameric helicase/translocase.

bioRxiv preprint doi: https://doi.org/10.1101/069559; this version posted August 16, 2016. The copyright holder for this preprint (which was not certified by peer review) is the author/funder. All rights reserved. No reuse allowed without permission.

## SIGNIFICANCE

Hexameric, ring-shaped translocases are molecular motors that convert the chemical energy of ATP hydrolysis into the physical movement of protein and nucleic acid substrates. Structural studies of several distinct hexameric translocases have provided insights into how substrates are loaded and translocated; however, the range of structural changes required for coupling ATP turnover to a full cycle of substrate loading and translocation has not been visualized for any one system. Here, we combine low- and high-resolution structural studies of the Rho helicase, defining for the first time the ensemble of conformational transitions required both for substrate loading in solution and for substrate movement by a processive hexameric translocase.

bioRxiv preprint doi: https://doi.org/10.1101/069559; this version posted August 16, 2016. The copyright holder for this preprint (which was not certified by peer review) is the author/funder. All rights reserved. No reuse allowed without permission.

## INTRODUCTION

Hexameric helicases and translocases are motor proteins that play a central role in cellular transactions ranging from replication and repair to transcriptional regulation, chromosome packaging, and proteolytic homeostasis (1-4). Used to drive the processive and at times highly-rapid movement of extended nucleic acid or protein chains through a central pore, ring-shaped motors face several challenges to their operation. One is that certain enzymes must transition through controlled ring opening and/or subunit assembly events to allow long, polymeric substrates that lack freely-accessible ends access to interior motor elements (5-7). Another is that, once loaded, the molecular plasticity inherent to these assemblies must be harnessed to precisely coordinate ATP binding and hydrolysis between multiple subunits for powering substrate translocation, while at the same time alternating between tight and loose grips on the substrate to allow for processive movement. The substrate-dependent molecular rearrangements that underpin ring dynamics during these events remain poorly understood not only for hexameric helicases and translocases, but for related ring-shaped switches as well.

The *E. coli* Rho transcription termination factor is a well-established model system for understanding hexameric translocase and helicase function (8, 9). During termination, Rho uses a cytosine-specific RNA binding domain appended to the N-terminus of a RecA-type ATPase fold (10, 11) to bind nascent RNA transcripts at cytosine-rich sequences (known as Rho utilization (*rut*) sites) (12, 13). Once loaded, Rho consumes ATP to translocate 5'→3' toward a paused RNA polymerase, eventually promoting transcription bubble collapse and RNA release (14-19).

Structural studies have provided insights into the mechanics of RNA loading by Rho, imaging the helicase in both closed-circular and notched/lockwasher-shaped states (20-24). These findings have suggested that Rho monomers assemble into a pliant hexamer that can spontaneously open to allow nucleic acid entry into the translocation pore (22, 24, 25), a property that has been observed in other hexameric helicases such as the eukaryotic MCM2-7 complex (26-28). By comparison, the structure of a closed-ring Rho complex bound to single-stranded RNA and the ATP-mimetic ADP•$BeF_3$ has provided a picture of a prospective translocation intermediate of the motor (29). This work, combined with that of a prior landmark model for the human papillomavirus E1 helicase bound to single-stranded DNA and ADP (30) (as well as more

bioRxiv preprint doi: https://doi.org/10.1101/069559; this version posted August 16, 2016. The copyright holder for this preprint (which was not certified by peer review) is the author/funder. All rights reserved. No reuse allowed without permission.

recent work on the replicative helicase, DnaB (31)), has led to two general principles for understanding hexameric helicase function. One is that, as proposed first for the T7 gp4 protein (32), hexameric helicases likely employ a sequential, rotary ATPase mechanism similar to that used by the F1 ATPase to power translocation (33). Another is that both the relative order of hydrolysis between subunits and/or differences in subunit orientation within a motor can determine the polarity of nucleic acid translocation (29, 30, 34, 35).

Despite present-day insights, there remain many unanswered questions regarding the loading and translocation mechanism of Rho. For example, there has been no systematic assessment of the extent to which the various crystallographic states observed thus far correlate with the predominant structures adopted by Rho in solution. The relative roles that ATP and RNA play in promoting ring opening *vs*. ring closing are similarly unresolved. At the same time, the range and types of movements that accompany ATP turnover events to support RNA translocation have yet to be fully defined. Likewise, it is unclear how the physical nature of the nucleic acid substrate itself – its chemical identity and base composition – feeds back to ATPase centers to influence motor activity. Answers to these questions are needed to understand fundamental aspects of hexameric helicase loading and translocation not just by Rho, but by hexameric motor proteins in general.

To better define the physical basis by which substrate-coupled conformational changes underpin hexameric motor mechanism, we conducted both solution and crystallographic structural studies of *E. coli* Rho with the goal of characterizing novel conformational intermediates in conjunction with different RNA sequences and nucleotide-binding modes. Small-angle X-ray scattering (SAXS) confirms that the current open- and closed-ring models imaged crystallographically correspond to the dominant states adopted in solution in the absence and presence of substrates, respectively, and further establish that Rho ring closure occurs only when both RNA and ATP are present. Three new crystal structures of Rho (including an experimentally-phased structure at higher resolution than that determined previously) reveal new ring rearrangements accompanying ATP cycling, which together with comparisons to other oligomeric RecA-family motors, uncover a common allosteric linkage that physically connects nucleic-acid binding with ATPase activation in members of this widespread motor family.

bioRxiv preprint doi: https://doi.org/10.1101/069559; this version posted August 16, 2016. The copyright holder for this preprint (which was not certified by peer review) is the author/funder. All rights reserved. No reuse allowed without permission.

Together, our data highlight unexpected sub-steps in the Rho loading/translocation cycle, and help explain previous research implicating RNA sequence as a regulator of Rho function in transcription termination (36-39).

## RESULTS

*Both RNA and ATP are required to drive Rho ring closure*

To probe how Rho physically and differentially responds to the binding of substrates such as nucleotide and RNA, we first used small angle X-ray scattering (SAXS) to verify whether the available crystal structures of the helicase correspond to major or minor population states in solution (**Fig. 1a-b and Supplementary Fig. 1a-b**) (40). SAXS data were initially collected on Rho in the absence of ligand, and on Rho mixed with one molar equivalent per hexamer of a poly-pyrimidine RNA ($rU_{12}$) and 2 mM ADP•$BeF_3$, a non-hydrolyzable ATP analog. Consistent with size-exclusion chromatography (**Supplementary Fig. 1c-d**), SAXS traces for Rho exhibited no sign of aggregation under any of the conditions tested, and distance distribution ($P_{(r)}$) profiles, Guinier analysis, and Kratky plots also were consistent with a well-behaved, hexameric particle (**Supplementary Fig. 2 and Supplementary Table 1**). Notably, data collected in the absence and presence of both RNA and ADP•$BeF_3$ proved to be extremely close matches to the theoretical curves calculated from models of the open and closed-ring structures of Rho, respectively (**Fig. 1a-b**). These data indicate that the open and closed-ring crystal structures seen previously for Rho indeed reflect the predominant conformations of native particles in solution.

To assess the individual contributions of RNA and nucleotide to ring closure, we next conducted SAXS experiments in either the presence or absence of RNA, and over several ADP•$BeF_3$ concentrations. Data collected in the absence of RNA but with 0, 0.5, 1, or 2 mM ADP•$BeF_3$ induced only modest changes in the scattering profile (**Supplementary Fig. 1a**). By contrast, scattering data collected in the presence of RNA exhibited distinct changes as ADP•$BeF_3$ concentrations were increased (**Supplementary Fig. 1b**). Data collected at intermediate concentrations of nucleotide could not be properly modeled by individual Rho crystal structures, so we used the programs FOXS and OLIGOMER to fit a two-component

bioRxiv preprint doi: https://doi.org/10.1101/069559; this version posted August 16, 2016. The copyright holder for this preprint (which was not certified by peer review) is the author/funder. All rights reserved. No reuse allowed without permission.

model consisting of both the open- and closed-ring Rho structures (**Supplementary Tables 2-3**) (41-43). The two-component analysis produced greatly improved fits, indicating that in the absence of RNA, ~92% of the Rho hexamers are open in solution, and that ~82% remain open even at high (2mM) ADP•$BeF_3$ concentrations (**Fig. 1c**). By contrast, with the addition of RNA, nucleotide titration leads to ring closing in Rho, such that by 2mM ADP•$BeF_3$, the hexamer population approaches 100% closed. Together, these data confirm that Rho forms an open lock-washer in solution, and further demonstrate that both RNA and nucleotide are required to promote ring closure (5). This RNA- and ATP-dependent conformational change in Rho may be the rate-limiting step previously observed in stopped-flow kinetics measurements of ATP hydrolysis (44), a notion that is supported by the noted acceleration of both ATPase and ring closure rates in response to primary site occupancy ((38) and (45)).

*A new closed-ring Rho state manifests a sequential shift in ATPase status*

Having established that existing crystallographic models are suitable representations of predominant Rho states in solution, we next set out to determine whether different substrate-bound, closed-ring forms of Rho might exist. We postulated that different RNA sequences or nucleotide-binding conditions might influence the formation of such intermediates. Since our initial closed-ring Rho crystals were difficult to work with (hereafter referred to as $Rho^{PolyU\text{-}P1}$, in reference to the RNA sequence and space group in which the protein crystallized) (46), we set out to find a new crystal packing arrangement that could be obtained in the presence of different RNA and nucleotide conditions, but that still possessed at least one complete Rho hexamer per asymmetric unit (so as to image the particle in the absence of crystal symmetry influences). We therefore conducted a new, broader set of screens with purified Rho in the presence of RNA and nucleotide, discovering a crystal form belonging to the spacegroup $P2_1$ that satisfied these criteria (**Methods**).

From the new Rho form, we were able to experimentally phase and refine a higher resolution (2.6 Å) structure of an intact hexamer bound to seven nucleotides of a centrally bound poly-U RNA, and that displayed electron density for ADP•$BeF_3$•$Mg^{2+}$ bound to all six ATP-binding sites (hereafter referred to as $Rho^{PolyU\text{-}P2_1}$) (**Fig. 2a-d and Table 1**). The experimental

bioRxiv preprint doi: https://doi.org/10.1101/069559; this version posted August 16, 2016. The copyright holder for this preprint (which was not certified by peer review) is the author/funder. All rights reserved. No reuse allowed without permission.

phases and higher resolution allowed us to correct two small building errors in previous Rho structures (**Supplementary Fig. 3**). A global alignment of the new $P2_1$ model with the original P1 state reveals that the two hexamers are highly similar structurally (**Fig. 2a**), with a root mean squared deviation (RMSD) for all shared backbone Cα atoms of 1.55 Å. As seen previously, five subunits of the $Rho^{PolyU\text{-}P2_1}$ state form a smoothly-ascending spiral staircase that wraps around a single-stranded RNA helix; the sixth (subunit F) occupies a "transit" position midway between the uppermost (A) and bottommost (E) protomers to close the ring (**Fig. 2b**). In addition, four classes of nucleotide-binding sites were again evident at the six intersubunit interfaces. Using criteria such as nucleotide B-factors (a measure of positional accuracy, or "orderedness" (47)) and coordination geometry, these sites have been classified as corresponding to either "exchange" (*E*), "ATP-bound" (*T*), "hydrolysis" (*T**), or product (*D*) states along the ATPase cycle (**Fig. 2a**) (29).

Globally, the conformations of the ATPase sites and the sequential order of ATPase states in the new $P2_1$ Rho model initially appeared similar to those seen in the original P1 structure, with the modeled nucleotides refining to a relative B-factor distribution consistent with the formation of three tight and three weak ATP-binding environments as observed biochemically (48-53) (**Supplementary Fig. 4**). However, inspection of the distance vectors calculated between Cα atoms for the P1 and $P2_1$ models revealed that subunit F, as well as the RNA binding R-loops of subunits E and A, have moved with respect to one other around a vector roughly parallel to the ring axis (**Figure 2e**).

Because the A, F and E subunits are thought to represent the likely sites for the release of nucleotide hydrolysis products and the binding of fresh ATP within the hexamer (29), we elected to compare the nucleotide-binding regions of the two Rho models in more detail. This analysis uncovered pronounced changes in some of the nucleotide-binding sites, which in turn revealed a shift in the pattern of functional states between the P1 and $P2_1$ forms of Rho (**Figs. 2a, 3**). The most striking change is that the presumptive catalytic water molecules seen in subunit A and B active sites of the initial closed ring structure now appear in the catalytic centers of subunits B and C in the new structure (**Fig. 2a, 3a-c and Supplementary Fig. 5a-c**). Moreover, each of these waters also has shifted its local position from a non-ideal location in the $Rho^{PolyU\text{-}P1}$ model

bioRxiv preprint doi: https://doi.org/10.1101/069559; this version posted August 16, 2016. The copyright holder for this preprint (which was not certified by peer review) is the author/funder. All rights reserved. No reuse allowed without permission.

to now take up a direct, in-line attack configuration with the $BeF_3$ group of the bound nucleotide in the $Rho^{PolyU\text{-}P2_1}$ structure (**Fig. 3b**). Repositioning of the waters is mediated at both interfaces by a conserved arginine (the "arginine-switch" (RS), R269), the catalytic glutamate (CE) residue (E211) that polarizes the water to assist hydrolysis, and a backbone carbonyl (G337) of the adjacent protomer. The glycine-mediated contact was not observed in the prior P1 Rho structure. Consistent with biochemical studies implicating their importance to overall Rho function (10, 54-58), a conserved network of ion-pairs at the B/C and C/D interfaces – which runs from the RNA-binding pore to the ATPase center – appears to help orient amino acids responsible for in-line placement of the attacking water (**Supplementary Fig. 6**). Overall, the new placement for the catalytic waters in $Rho^{PolyU\text{-}P2_1}$, together with other changes in the relative orientations of catalytic important amino acids (**Fig. 3a-f and Supplementary Discussion**), supports the proposed existence of hydrolysis-competent active sites in the closed-ring Rho states (29). This shift also advances the relative position of the two *T** states by one subunit toward the lone *E*-state, and adds a second *D*-state compared to the $Rho^{PolyU\text{-}P1}$ structure determined previously (**Fig. 2a**).

*Inter-subunit relationships in the nucleotide-exchange region mirror those of an open-ring state*

A key supposition of the rotary cycling model based on the polyU-bound P1 Rho crystal form has been that the E/F interface, which is relatively open and solvent exposed, corresponds to a nucleotide exchangable (*E*) site where substrate can bind to or product can dissociate from the hexamer, respectively (29). To test this idea, we back-soaked nucleotide out of the new $Rho^{PolyU\text{-}P2_1}$ crystal form and determined the structure of the helicase by X-ray crystallography. Inspection of all active sites in the model revealed very weak and discontinuous electron density for the nucleotide-binding site of subunit E, indicating a very low occupancy for ADP•$BeF_3$ that precluded modeling of nucleotide into the site (nucleotide density in the other active sites was unchanged) (**Fig. 4a-b**). Intersubunit distance vectors calculated between the back-soaked structure (referred to hereafter as $Rho^{Empty}$) and the fully occupied $Rho^{PolyU\text{-}P2_1}$ structure show that the relative positions of subunits E and F shift by ~1.7 Å with respect to one another, but that the rest of the subunits in the hexamer undergo only minor positional changes (**Fig. 4c**). A comparison of the E/F interface in the presence and absence of ADP•$BeF_3$ reveals an increased separation of the two subunits that moves the Arg-finger out of the active site and that buries

bioRxiv preprint doi: https://doi.org/10.1101/069559; this version posted August 16, 2016. The copyright holder for this preprint (which was not certified by peer review) is the author/funder. All rights reserved. No reuse allowed without permission.

~120Å$^2$ less total surface area at the interface (**Fig. 4d**). Together, these observations further confirm the proposition that the E/F active site corresponds to a nucleotide-exchange point, and show that product release coincides with an increased opening of the subunit interface at this catalytic center. Interestingly, upon the disappearance of nucleotide from the *E*-state, the relative B-factors for the nucleotide in the active site of subunit F also increased relative to other Rho structures (**Supplementary Fig. 4**), suggesting that product release may cooperatively weaken the association of nucleotide in the immediately adjacent *D*-state.

Inspection of the E/F active site shows that the *E*-state is unique within the closed-ring Rho hexamer in adopting a relative intersubunit orientation markedly different from that of the other protomers. This altered configuration arises due to a transition of subunit F (which is bounded by subunits A and E, respectively) from the top step of the helical RNA staircase to the bottom (**Fig. 2b**). Subunit F is also the only protomer that does not contact RNA in any closed-ring structure determined so far, and its interface with subunit E in the Rho$^{Empty}$ structure represents a completely substrate-free component of the catalytic cycle. Given these considerations, we compared the intersubunit positions of the E/F protomer conformation of the back-soaked model with those of a completely RNA-free, open-ring Rho structure of Rho determined previously. Interestingly, the intersubunit orientation of motor domains in the open-ring structure (PDB: 1PVO), which all assemble with a left-handed helical pitch, proved to be a very close match to the orientation of the E/F protomer pair in both the Rho$^{Empty}$ and Rho$^{PolyU\text{-}P2_1}$ structures, but distinct from other subunit dimers in the RNA-bound models (which adopt a right-handed pitch) (**Fig 4e**). This congruency indicates that, upon ATPase product and RNA release, a single interface in the Rho hexamer relaxes to an energetically favorable conformation present in the open-ring Rho structure. Therefore, the nucleotide-dependent structural transition, which promotes ring opening and closing during RNA loading, also plays a direct role in catalytic cycling.

*Sequence and ATPase state-specific differences in RNA binding by Rho*

The ATPase activity of *E. coli* Rho has been well-established to depend not just on RNA binding (59), but also on RNA sequence, with pyrimidine-rich RNAs providing a greater

bioRxiv preprint doi: https://doi.org/10.1101/069559; this version posted August 16, 2016. The copyright holder for this preprint (which was not certified by peer review) is the author/funder. All rights reserved. No reuse allowed without permission.

increase in ATP turnover compared to purine-rich substrates (37, 38). To better understand this dependency, we crystallized and determined the structure of Rho in complex with a poly-purine RNA ($rA_{12}$) and ADP•$BeF_3$ (hereafter referred to as $Rho^{PolyA}$ ), and compared it to the other Rho structures determined thus far (**Fig. 5**). Notably, the Rho•poly-A complex co-crystallized in the same $P2_1$ space group and unit cell as the new closed-ring Rho model bound to poly-U. The poly-A substrate similarly forms an overwound, single-stranded RNA helix in the Rho pore that is highly similar to that formed by poly-U (**Fig. 5 and Supplementary Fig. 7**), despite the extra bulk afforded by the additional five-member ring on the purine bases. This finding indicates that the tight coiling of RNA seen in the original Rho model is not an effect of RNA sequence or crystal packing, but likely reflects the standard manner by which the helicase encircles substrate during translocation.

Close inspection of the poly-A Rho model with its poly-U counterparts reveals notable differences in the specifics of RNA binding. Interestingly, these differences are evident not just between purine- and pyrimidine-bound Rho hexamers, but also between the different poly-U models imaged thus far (**Fig. 5a-c**). In particular, the $Rho^{PolyU\text{-}P2_1}$ and $Rho^{PolyA}$ structures lack electron density for the 5'-most base present in original $Rho^{PolyU\text{-}P1}$ structure, and instead manifest new density for two additional bases at the 3'-end of the RNA (**Fig. 5 and Supplementary Fig. 7b-g**). However, the bound RNAs also show conformational differences between these three structures, with the additional 3' nucleotides visible in the poly-A bound Rho model extending in a straight line from the helicase pore, but in the new poly-U structures folding back into a tight kink that deviates from the interior RNA spiral configuration but maintains base-stacking interactions (**Fig. 5 and Supplementary Fig. 7**). The U-U kink seen in the poly-U models allows for a network of contacts to be formed between the ribose 2'-OH and the uracil O2 atom of the penultimate nucleotide, a newly evident water molecule, and Lys326 of both subunits B and C (the latter of which alters the contact that had seen previously between this invariant amino acid and the backbone phosphate of RNA in the original $Rho^{PolyU\text{-}P1}$ hexamer) (**Fig. 5a-c, Supplementary Fig. 8**). Interestingly, in analyzing the $Rho^{Empty}$ structure, we observed electron density for the additional, kinked 3' bases of RNA similar to that present in $Rho^{PolyU\text{-}P2_1}$; however, this model also exhibited density for the 5'-most base seen in $Rho^{PolyU\text{-}P1}$ (**Fig. 5b and Supplementary Fig. 7b-d**). Thus, upon loss of nucleotide and opening of the *E*-

bioRxiv preprint doi: https://doi.org/10.1101/069559; this version posted August 16, 2016. The copyright holder for this preprint (which was not certified by peer review) is the author/funder. All rights reserved. No reuse allowed without permission.

state active site, the poly-U RNA bound to $Rho^{Empty}$ appears to adopt a hybrid conformation between the original $Rho^{PolyU\text{-}P1}$ crystal form and the new Rho-$P2_1$ crystal form.

Concomitant with the distinct 5'- and 3'-end structures of different bound RNAs, specific protein-RNA contacts also undergo a change. Overall, the new poly-U and poly-A models form a similar number of total polar contacts between Rho and RNA when compared to the prior $Rho^{PolyU\text{-}P1}$ structure, but these frequently involve different residues. In addition to the changes in Lys326 noted above, Thr286 of Rho's Q-loop (the L1-loop equivalent of DnaB and T7 gp4) loses its interaction with the phosphate of RNA that was seen in the original closed-ring structure of Rho, leading both the backbone amide (not observed in $Rho^{PolyU\text{-}P1}$) and carbonyl (observed in $Rho^{PolyU\text{-}P1}$) groups of Val284 to shift and make a new contact with the 2'-OH of its associated ribose (**Fig. 5a-d**). These three models also manifest a slightly steeper RNA coil that is less compressed compared to the RNA seen previously in the P1 Rho model, likely due to changes in the intersubunit orientations between protomers E/F and F/A (**Fig. 2e and Supplementary Fig. 7**).

*A conserved allosteric helix coordinates crosstalk between subunits and their catalytic centers*

In considering how changes in the ATPase centers of our closed-ring Rho models might be coupled to RNA binding, we used the higher-resolution structures determined here to look more closely at the linkages that mediate intersubunit contacts between the nucleic acid and nucleotide binding sites. By co-aligning all six pairwise interfaces of the $Rho^{PolyU\text{-}P2_1}$ model, using the ATP-binding P-loop as an reference point, we found that a single α-helix (Rα1), which contains residues responsible for forming the salt-bridge network linking the RNA binding pore to the ATPase center, undergoes a large range of previously-unnoticed hinge movements (**Fig. 6a and Supplementary Fig. 6**). The N-terminus of this helix (which corresponds to the "R-loop" of Rho and the "L2"-loop of RecA helicases such as DnaB and T7 gp4) binds RNA via K326 (**Fig. 5**), while the C-terminus of this helix contains backbone carbonyls that interact directly with the catalytic water molecule and the arginine-based γ-phosphate sensors in the two T* states (**Figs. 3b and 6b**). This movement appears to be caused by an intersubunit levering motion of ~10Å at the helix's N-terminus, which alters the interactions in an ordered manner that correlates with the ATPase state of each subunit (**Fig. 6b and Supplemental Movie 1**). This observation

bioRxiv preprint doi: https://doi.org/10.1101/069559; this version posted August 16, 2016. The copyright holder for this preprint (which was not certified by peer review) is the author/funder. All rights reserved. No reuse allowed without permission.

suggests that R-loop mediated RNA binding, aided by interactions within an intersubunit allosteric network, not only positions the catalytic glutamate via the arginine switch residue as described previously (29), but also directly controls the position the arginine finger, arginine valve, and catalytic water by coupled movements with associate Rα1 helix.

In conducting this analysis, we note that the α-helix corresponding to Rα1 is a conserved feature of the RecA fold, and is present not only in Rho's closest homolog (the $F_1$-ATPase, (60)), but also in more distantly related RecA-family hexameric helicases and translocases. In all cases, the C-terminal carbonyls of the helix equivalent to Rα1 contact amino acids that interact with the γ-phosphate moiety (and catalytic waters when present), and that appear poised to help control the active-site organization of their respective hexameric motors through a similar mechanism (**Fig. 6c-e**) (31, 60, 61). These comparisons indicate that this helix, which lies downstream of the R/L2 loop region, is likely involved in allosterically coupling substrate movements to ATPase status in RecA-like motors in general.

## DISCUSSION

### *A possible role for ring distortion and strain in the mechanism of Rho and other hexameric motors*

In the present study, we have used solution-based structural methods and X-ray crystallography to better understand how a RecA-family hexameric motor protein, Rho, couples changes in nucleotide status to conformational transitions that underpin ring loading and translocation events. Our SAXS data confirm that two distinct open- and closed-ring structures are accessed prior to and following RNA engagement, respectively (**Fig. 1a-c**), suggesting that the transition between these two states likely occurs as a relatively simple rigid body rotation of subunits with respect to each other (**Supplemental Movie 2**). Notably, our studies indicate that at nucleotide concentrations approaching those in the cell (values between 2 and 10 mM ATP have been measured for *E. coli* (62-64)), Rho spontaneously and preferentially occupies an open-ring state, a form that is well-suited for engaging nascent RNA transcripts. A need for contacts engendered by both substrate nucleic acid and ATP binding to cooperatively induce ring closure

bioRxiv preprint doi: https://doi.org/10.1101/069559; this version posted August 16, 2016. The copyright holder for this preprint (which was not certified by peer review) is the author/funder. All rights reserved. No reuse allowed without permission.

is consistent with the idea that formation of a translocation-competent state may capture and harness strain as a motive force to help promote nucleotide cycling. Consistent with this model, the formation of a relaxed, left-handed inter-subunit orientation characteristic of the open-ring structure is seen only in the product release state, which also releases its grip on RNA to reset the RNA binding cycle (**Fig 4e**).

Strain imparted by substrate-induced conformational changes may underlie ATP cycling in other, more distantly-related hexameric helicases. For example, recent structures of DnaB-family helicases have shown that the ATPase domains of these hexameric motors adopt an uncoupled, planar conformation in the absence of nucleic acid substrate (65), but form a steep right-handed helical conformation with a single open interface when DNA and GDP•$AlF_4$ are present (31, 65). Electron microscopy data on the eukaryotic minichromosome maintenance proteins (MCMs) have revealed that a left-handed open-ring conformation is the default state of metazoan MCM hexamers (27), and that the Cdc45•GINS complex, along with ATP and DNA are needed to drive the formation of a stable closed ring with an internal, right-handed pitch (26, 34). Together, these studies support the idea that nucleic acids cooperatively activate ATP hydrolysis in ring-shaped many RNA and DNA translocases by serving as a template for the asymmetric assembly of ATPase subunits. This asymmetry in turn promotes the formation of a defined sequence and order of active site states (29, 30), which allows the energetics of cooperative substrate binding in one subunit to be allosterically coupled to cooperative product release in another. One exception to this trend may be the papilloma virus E1 helicase, which has been found to adopt an asymmetric, right-handed closed ring in the absence of ATP and DNA (66).

*RNA sequence dependencies of the Rho functional cycle*

In addition to the insights afforded into ring dynamics and the establishment of a sequential ATPase order, the structures presented here also help to explain some of the known effects that RNA sequence has on Rho's ATPase activity. In general, the molecular basis for substrate-specific sequence dependencies in hexameric helicases and translocases has remained relatively ill-defined. Some ring-shaped helicases, such as T7 gp4, decelerate when confronted with GC-rich duplexes (67), indicating that motor function can be impacted by substrate stability.

bioRxiv preprint doi: https://doi.org/10.1101/069559; this version posted August 16, 2016. The copyright holder for this preprint (which was not certified by peer review) is the author/funder. All rights reserved. No reuse allowed without permission.

For Rho, transcription termination activity is stimulated by cytosine-rich sequences (13), due in part to the recognition requirements of its primary RNA (*rut*)-binding sites (10, 38), and also to the ability of primary site occupancy to promote Rho ring closure (see accompanying study (45)). However, Rho's RNA-stimulated ATPase and translocation activities also appear to be directly affected by pyrimidine-specific sequence preferences independent of primary site interactions (36-38).

The differences in secondary site RNA binding seen here between poly-U and poly-A bound forms of Rho (along with the preferential ring closure capability of poly-U over poly-A described in the accompanying study (45)) indicate that sequence discrimination in the helicase may in part arise from interrogation of RNA sequence at the point where the nucleic acid threads into the ring. In particular, the 3' kink seen in the new Rho$^{\text{PolyU-P2}_1}$ structure allows a ribose 2'-OH and two pyrimidine bases to interact with an invariant lysine, Lys326, on two different R-loops. These contacts are absent in the 3' RNA region when Rho is bound to poly-A, and in the original Rho$^{\text{PolyU-P1}}$ model (where the 3' nucleotides are unstructured, see **Fig. 5**). Intriguingly, the lysines involved in binding the U-U kink in Rho$^{\text{PolyU-P2}_1}$ project from subunits B and C, which also manifest the two *T** states observed in the hexamer (**Fig. 2a**). These interactions suggest that Lys326, in addition to its role neutralizing the backbone charge of RNA bound in Rho's translocation pore (29), may also serve as a sensor for RNA sequence to help properly organize the B- and C-subunit active sites (**Fig. 3a**). Such a function would explain why pyrimidine-rich *rut* sites are particularly well-suited as secondary site ligands to promote nucleotide hydrolysis by Rho, in that they provide an RNA structural motif that helps set up an idealized ATPase configuration.

The differences in the 3' RNA structure seen here for the purine and pyrimidine substrates likewise have implications for understanding how RNA sequence is coupled to step size. For instance, using nucleotide analog interference mapping (NAIM) to insert dNTPs into RNA, Rho has been found to be inhibited by the presence of deoxyribose at intervals of every seven nucleotides, with the level of inhibition dependent on the local sequence environment (36). Our structures reveal that pyrimidine, but not purine substrates can specifically interact with Lys236 of Rho by forming a specific kink that involves the 2'OH and pyrimidine base of the

bioRxiv preprint doi: https://doi.org/10.1101/069559; this version posted August 16, 2016. The copyright holder for this preprint (which was not certified by peer review) is the author/funder. All rights reserved. No reuse allowed without permission.

incoming 3'-RNA end (**Fig. 5**). Given that movements of the R-loop are directly coupled to changes in the allosteric network that couples ATPase status with RNA-binding (**Figs. 6 and Supplementary Fig. 6**) (29), the ability to adopt a kink by pyrimidines may help underpin the positional and sequence dependency of the 2'-OH activation step seen to occur roughly every seven steps by NAIM (36, 68).

*Structural snapshots reveal translocation sub-steps in a hexameric motor protein.*

The present study provides the most comprehensive structural analysis to date for a hexameric helicase bound to different nucleic acid substrates and nucleotide intermediates. In comparing the original P1 and the new $P2_1$ poly-U bound models of Rho, both hexamers can be seen to possess a single *E*-state active site (subunit E) that sits adjacent to a *T* (ATP-bound) state ATPase center (subunit D). The two structures diverge, however, in that the $Rho^{PolyU\text{-}P1}$ form contains a second *T*-state active site (subunit C) followed by two hydrolysis-like *T** states (subunits B and A), whereas the $Rho^{PolyU\text{-}P2_1}$ model is shifted, possessing a lone *T*-state followed immediately by two *T** catalytic centers (**Fig. 2**). As a consequence, the $Rho^{PolyU\text{-}P1}$ structure contains only a single product (*D*) state (subunit F), whereas the corresponding $Rho^{PolyU\text{-}P2_1}$ structure contains two (subunits F and A). This observation is consistent with prior studies showing that there exists a 2-4 subunit delay in ATP hydrolysis and product release in Rho and related RecA-family hexameric helicases such as T7 gp4 (see (69) and **Supplementary Discussion**).

Although the *E*-state active site (subunit E) remains the most solvent-accessible ATPase center in both crystal forms of Rho, changes in the relative disposition of key functional amino acids are nonetheless evident for this region between the P1 and $P2_1$ structures. In particular, the subunit E active site of the new $Rho^{PolyU\text{-}P2_1}$ model exhibits a dramatically displaced and off-line catalytic glutamate, but forms a new contact between the arginine-finger and the $BeF_3$ moiety; by contrast, in the original $Rho^{PolyU\text{-}P1}$ structure, the correct positioning of the catalytic glutamate is maintained but the arginine-finger/nucleotide contact is broken (**Fig. 3d-e**). Concomitant with these changes, two bases at the 3' end of the bound RNA become ordered and coordinated in the $Rho^{PolyU\text{-}P2_1}$ structure, whereas in the $Rho^{PolyU\text{-}P1}$ model, only a single extra base is apparent at the 5' RNA end (**Fig. 5**). Interestingly, back-soaking of the new poly-U Rho crystal form, which

bioRxiv preprint doi: https://doi.org/10.1101/069559; this version posted August 16, 2016. The copyright holder for this preprint (which was not certified by peer review) is the author/funder. All rights reserved. No reuse allowed without permission.

results in nucleotide dissociation from the E-subunit interface, produces a hybrid state in which RNA density is evident at both 5' and 3' ends.

Taken together, the suite of Rho structures not only recapitulates the movements expected for 5'→3' translocation along RNA, but also highlights the existence of sub-steps within the context of a sequential ATPase mechanism (**Figure 7 and Supplemental Movie 3**). In this scheme, formation of an empty ATPase center would promote downstream (3') contacts between Rho and its substrate, while maintaining 5' interactions leftover from the prior round of hydrolysis. ATP binding would next disrupt the 5' RNA contact, initiating a new translocation cycle to pull the 3' end of the bound RNA into the motor pore. Finally, product formation would complete the translocation step, helping to shepherd the 5' RNA end out of the helicase, after which ADP release would reset the system by forming new contacts to the incoming 3' base.

Although conformational substeps have been observed structurally for superfamily 1 and 2 helicases and for motors such as the F1 ATPase, myosin, and kinesin (70-73), similar insights have not been forthcoming for hexameric helicase/translocase systems. Functional substeps (as well as macrosteps) are frequently observed in single molecule studies of motor proteins (74, 75), but the architectural underpinnings of these events often remained unresolved. The present work demonstrates the existence of distinct physical substates in a RecA-family hexameric helicase, and moreover implicates both RNA binding and different stages of the ATPase cycle in the formation and dissolution of these states. Future efforts involving high-resolution single-molecule studies and structure-guided mutagenesis will help establish the timing by which different states interconvert with each other and the role that specific, protein-mediated contacts between RNA and ATP play in controlling these transitions.

bioRxiv preprint doi: https://doi.org/10.1101/069559; this version posted August 16, 2016. The copyright holder for this preprint (which was not certified by peer review) is the author/funder. All rights reserved. No reuse allowed without permission.

## METHODS

*Small Angle X-ray Scattering (SAXS) data collection and analysis.*

Native Rho protein was prepared in a similar manner to selenomethionine-labeled protein as described (22). Rho protein (40 mg/mL) in size exclusion buffer (50 mM Tris 7.5, 500 mM KCl, 10% Glycerol, 1mM TCEP) was dialyzed overnight into SAXS buffer (150 mM KCl, 50 mM HEPES pH 7.5, 5 mM $MgCl_2$, 5% Glycerol). Dialyzed protein was then further diluted to 5 mg/mL in SAXS buffer containing various concentrations of RNA (rU12) or ADP•$BeF_3$, aliquoted into a 96 well plate, and used for data collection at room temperature using an automated system at ALS Beamline 12.3.1. Raw SAXS data were integrated, scaled, and buffer subtracted with the program OGRE (Greg Hura, Lawrence Berkeley National Laboratory). PRIMUS was used to merge data from a one second and ten second exposure and to manually remove outliers near the beam-stop in order to obtain high quality scattering curves with very little noise (76). Guinier analysis was performed using AUTORG (77). Distance distribution functions (P(r)), maximum diameters ($D_{max}$) and real- and reciprocal-space radius of gyration ($R_g$) values were calculated with GNOM (78). Structural models were generated using an open-ring Rho model (PDB: 1PVO (22)) and the closed ring crystal structure determined here ($Rho^{PolyU\text{-}P2_1}$). Missing loops or domains were added to the structural models by superposition with other structures or subunits containing the missing residues. OLIGOMER and FOXS were used to compare theoretical scattering curves to the data and compute the relative contributions of multi-component datasets (42, 43, 79). Background subtraction as implemented in FOXS or OLIGOMER was used to account for errors in buffer composition and improve the fit of the high-resolution data.

*Protein crystallization and data collection.*

Selenomethionine labeled *E. coli* Rho protein was prepared, and the RNA-ADP•$BeF_3$ complexes were formed as described previously (22, 29), except that Rho was dialyzed into a buffer containing 10 mM Tris pH 7.5, 100 mM NaCl and 0.5 mM TCEP prior to complex formation. RNA (rU12 and rA12 polymers) was purchased from IDT. Rho was crystallized by mixing 250 nL of Rho complex (20 mg/mL) with 250 nL of a well solution containing 200 mM KOAc, 40% MPD and 0.5% ethyl acetate using a Mosquito Nanoliter Pipetting system (TTP Biotech), in a

bioRxiv preprint doi: https://doi.org/10.1101/069559; this version posted August 16, 2016. The copyright holder for this preprint (which was not certified by peer review) is the author/funder. All rights reserved. No reuse allowed without permission.

hanging-drop vapor diffusion format. Crystals grew within three days and reached maximum size within one week. Crystals were harvested directly by looping and plunging in liquid nitrogen. Crystals were mounted on bendable cryo-loops (Hampton Research), oriented to minimize spot overlap, and used for collecting diffraction data on Beamline 8.3.1 at the Advanced Light Source (80). Diffraction data from the new $Rho^{PolyU\text{-}P2_1}$ crystal form were significantly improved compared to the previous $Rho^{PolyU\text{-}P1}$ model (29), displaying lower mosaicity (~1° *versus* 2°), and higher resolution (2.6 Å *versus* 2.8 Å). Co-crystals of Rho with a short poly-adenosine RNA ($rA_{12}$) and ADP•$BeF_3$ were obtained under nearly identical conditions by substituting $rA_{12}$ RNA for $rU_{12}$ RNA during rho complex formation. To obtain the $Rho^{Empty}$ crystals, we first grew $Rho^{PolyU\text{-}P2_1}$ crystals, and then conducted stepwise exchange of the mother liquor with an identical solution containing no ADP•$BeF_3$. After a series of 2-fold dilutions and equilibrations conducted over ~15 minutes, the concentration of ADP•$BeF_3$ in the mother liquor was reduced approximately 30-fold (further dilution caused the crystals to dissolve).

*Structure solution and refinement.*

All data were processed in HKL-2000 (81). Molecular replacement/ single wavelength anomalous dispersion (MR/SAD) methods as implemented in PHENIX were used to phase the $Rho^{PolyU\text{-}P2_1}$ structure (82). Molecular replacement was conducted using a monomer from the $Rho^{PolyU\text{-}P1}$ structure. Phases from the resulting solution were used by the program PHASER to locate 92 selenium sites in the asymmetric unit and phase the structure using SAD (83), producing a figure of merit (FOM) of 0.39 for unmodified phases. Multi-domain, six-fold non-crystallographic symmetry (NCS) averaging and phase extension into an isomorphous, low-energy remote dataset using RESOLVE produced a FOM of 0.63 (84). These high quality maps allowed us to clearly locate bound ligands (**Fig. 2c-d and Supplementary Fig. 6a-i**) and correct small errors in previous structures (**Supplementary Fig. 3**). The final model, which was refined to an $R_{work}/R_{free}$ of 21.8/24.6%, currently represents the highest resolution view of a hexameric helicase bound to both nucleic acid and an ATP mimic. The Ramachandran statistics for this model are 98.17% favored, 1.79% allowed, and 0.04% outliers as reported by MOLPROBITY (85).

The nearly isomorphous $Rho^{Empty}$ and $Rho^{PolyA}$ structures were solved by molecular replacement, using the entire $Rho^{PolyU\text{-}P2_1}$ structure as a search model, and $R_{free}$ was calculated

bioRxiv preprint doi: https://doi.org/10.1101/069559; this version posted August 16, 2016. The copyright holder for this preprint (which was not certified by peer review) is the author/funder. All rights reserved. No reuse allowed without permission.

using the same test set for all structures. Rigid body refinement of the N (1-126) and C (127-417) terminal domain of each individual subunit was conducted following molecular replacement for all structures. The structures were refined in PHENIX using custom bond and angle restraints for the bound ADP•$BeF_3$ complex, individual ($Rho^{PolyU\text{-}P2_1}$) or group ($Rho^{PolyA}$ and $Rho^{Empty}$) B-factor modeling, and TLS modeling using selections obtained from the TLSMD server (82, 86). The $Rho^{PolyA}$ structure was refined to 3.15 Å with an $R_{work}/R_{free}$ of 23.3/26.5%, contains six bound ADP•$BeF_3$•$Mg^{2+}$ moieties and resolves seven bases of poly-adenosine RNA (**Table 1 and Supplementary Figure 5f-g**). The Ramachandran statistics for this structure are 97.48% favored, 2.52% allowed, and 0% outliers. The $Rho^{PolyA}$ model closely aligns with both the $Rho^{PolyU\text{-}P1}$ and $Rho^{PolyU\text{-}P2_1}$ structures (RMSDs of 1.57 Å and 0.82 Å respectively for backbone C-α atoms). The $Rho^{Empty}$ structure was refined to 3.2 Å resolution with an $R_{work}/R_{free}$ of 23.2/26.6%, contains five clearly resolved ADP•$BeF_3$•$Mg^{2+}$ complexes and resolves eight bases of poly-U RNA (**Table 1 and Supplementary Figure 5h-i**). The Ramachandran statistics for this structure are 97.68% preferred, 2.32% allowed, and 0% outliers. The structure displays the largest changes in overall architecture compared to the other Rho states, aligning with $Rho^{PolyU\text{-}P1}$, $Rho^{PolyU\text{-}P2_1}$and $Rho^{PolyA}$ structures with Cα RMSDs of 2.39 Å, 0.82 Å, and 0.88 Å respectively.

*Structural analysis.*

All figures were prepared using PYMOL (Schrödinger). Structural superpositions were conducted with the CEALIGN PYMOL plugin (87). Energy minimized linear interpolations were computed using a CNS script written by the Yale Morph Server (88). To place atomic B-factors from different structures on the same relative scale (**Supplementary Figure 4**), atomic B-factors for each structure were divided by the average B-factor for that structure and then multiplied by the average B-factor for all structures. Distance vectors calculated between various Rho structures were calculated as described (89). Vector length corresponds to distances between Cα atoms among different structures multiplied by a scale factor of three to assist visualization, while vector color corresponds to relative distance (dark blue: 0 Å; red: 1.5 Å or greater).

*Accession codes.*

Crystallographic data and structural models for $Rho^{PolyU\text{-}P2_1}$, $Rho^{PolyA}$ and $Rho^{Empty}$ have been deposited into the Protein Data Bank under accession codes 5JJI, 5JJK, and 5JJL respectively.

bioRxiv preprint doi: https://doi.org/10.1101/069559; this version posted August 16, 2016. The copyright holder for this preprint (which was not certified by peer review) is the author/funder. All rights reserved. No reuse allowed without permission.

## ACKNOWLEDGEMENTS

The authors thank Berger lab members for helpful discussions, Greg Hura and Dina Schneidman-Duhovny for guidance on SAXS data processing, Jamie Cate for assistance with distance vector calculations, Jane Tanamachi, George Meigs and James Holton at ALS Beamline 8.3.1, and Michal Hammel at ALS Beamline 12.3.1 for assistance with SAXS data collection. This research was supported by funding from the G. Harold and Leila Y. Mathers Foundation and the NIH (GM071747).

## AUTHOR CONTRIBUTIONS

NDT and JMB designed the study; QS identified the new Rho $P2_1$ crystallization condition; LBW performed protein purification, crystallization, and back-soaking to obtain the $Rho^{PolyA}$ and $Rho^{Empty}$ crystals; NDT performed all other protein purification and crystallization experiments, prepared SAXS samples, collected and analyzed all X-ray data, and solved and refined all structures. NDT, MRL, and JMB wrote the paper.

## COMPETING FINANCIAL INTERESTS

The authors declare no competing financial interests.

bioRxiv preprint doi: https://doi.org/10.1101/069559; this version posted August 16, 2016. The copyright holder for this preprint (which was not certified by peer review) is the author/funder. All rights reserved. No reuse allowed without permission.

**Table 1.** Data collection, phasing and refinement.

| | $Rho^{PolyU\text{-}P2_1}$ | $Rho^{PolyU\text{-}P2_1}$ | $Rho^{PolyA}$ | $Rho^{Empty}$ |
|---|---|---|---|---|
| **Data collection** | | | | |
| Space group | $P2_1$ | $P2_1$ | $P2_1$ | $P2_1$ |
| Cell dimensions | | | | |
| *a*, *b*, *c* (Å) | 68.72, 198.8, 111.8 | 69.00, 198.6, 111.4 | 68.76, 199.2, 112.2 | 69.09, 199.1, 111.7 |
| $\alpha, \beta, \gamma$ (°) | 90.0, 104.8, 90.0 | 90.0, 104.4, 90.0 | 90.0, 104.8, 90.0 | 90.0, 105.0, 90.0 |
| | *peak* | *remote* | *remote* | *remote* |
| Wavelength | 0.9796 | 1.116 | 1.116 | 1.116 |
| Resolution (Å) | 50-2.95 (3.06-2.95) | 50-2.60 (2.69-2.60) | 50-3.15 (3.26-3.15) | 50-3.2 (3.31-3.20) |
| $R_{sym}$ or $R_{merge}$ | 9.1 (46) | 8.1 (63) | 12.1 (60) | 12.8 (58) |
| $I/\sigma I$ | 10.8 (2.4) | 14 (1.8) | 9.4 (2.0) | 8.1 (1.8) |
| Completeness (%) | 98.2 (97.1) | 99.7 (99.1) | 99.0 (99.5) | 96.2 (96.4) |
| Redundancy | 5.6 (5.2) | 3.1 (3.1) | 2.9 (2.9) | 2.8 (2.8) |
| | | | | |
| **Refinement** | | | | |
| Resolution (Å) | | 47.4-2.6 | 49.8-3.15 | 49.5-3.2 |
| No. reflections | | 88,380 | 49,848 | 46,060 |
| $R_{work}/R_{free}$ | | 21.8 / 24.6 | 23.3 / 26.5 | 23.2 / 26.6 |
| No. atoms | | | | |
| Protein | | 19,164 | 18,696 | 18,888 |
| Ligand/ion | | 341 | 347 | 325 |
| Water | | 271 | 19 | 15[a] |
| B-factors | | | | |
| Protein | | 67.9 | 80.7 | 73.7 |
| Ligand/ion | | 53.6 | 69.9 | 66.6 |
| Water | | 45.2 | 64.5 | 46.6 |
| R.M.S deviations | | | | |
| Bond lengths (Å) | | 0.006 | 0.006 | 0.006 |
| Bond angles (°) | | 0.575 | 0.560 | 0.691 |

Values in parenthesis correspond to the highest resolution bin

[a]Only waters involved in octahedral coordination of the active site $Mg^{2+}$ ions were modeled

bioRxiv preprint doi: https://doi.org/10.1101/069559; this version posted August 16, 2016. The copyright holder for this preprint (which was not certified by peer review) is the author/funder. All rights reserved. No reuse allowed without permission.

## FIGURE LEGENDS

**Figure 1.** SAXS analysis of apo and substrate-bound Rho complexes. (a) Scattering curve for apo Rho in solution (blue) closely matches the theoretical curve (red) calculated from a model based on the open-ring structure (1PVO, inset (22)), but not the theoretical curve (black) calculated from a closed ring-Rho model bound to RNA and ADP•$BeF_3$. (b) Scattering curve for Rho in the presence of RNA (1:1 RNA:hexamer) and 2 mM ADP•$BeF_3$ (pink) closely matches the theoretical curve (black) calculated from the closed ring-Rho structure bound to RNA and ADP•$BeF_3$ determined here but not the theoretical curve (red) calculated from a open ring Rho model (1PVO). (c) Plot of the percent-closed value obtained with FOXS *versus* ADP•$BeF_3$ concentration shows that both RNA and ATP are required for Rho ring closure.

**Figure 2.** Overall structure and ligand binding in a new Rho translocation intermediate. (**a**) Superposition of a new Rho•RNA•ADP•$BeF_3$ structure ($Rho^{PolyU\text{-}P2_1}$, colored and labeled by subunit), with the previously-determined Rho•RNA•ADP•$BeF_3$ structure ($Rho^{PolyU\text{-}P1}$, white). Presumptive ATP hydrolysis states (*T* – ATP bound, *T** – ATP hydrolysis, *D* – product, *E* – exchange) are labeled in color ($Rho^{PolyU\text{-}P2_1}$) or white ($Rho^{PolyU\text{-}P1}$). (**b**) Schematic of closed-ring Rho hexamer (flattened on page) bound to RNA (one complete turn) highlighting the right-handed helical rise of the A/B/C/D/E interfaces that are bound to RNA, and the position of subunit F in transition between the top and bottom steps of the RNA binding staircase. Subunit C is shown twice to connect the two sides. (**c**) Experimental (density modified, SAD phased, $Rho^{PolyU\text{-}P2_1}$) electron density around one of the bound nucleotides (ADP – magenta, $BeF_3$ – black, $Mg^{2+}$ – yellow-green). (**d**) Experimental (density modified, SAD phased, $Rho^{PolyU\text{-}P2_1}$) electron density around the bound RNA (orange). (**e**) Intersubunit distance vectors calculated independently for each intersubunit interface between the $Rho^{PolyU\text{-}P1}$ and $Rho^{PolyU\text{-}P2_1}$ structures. Vectors were calculated relative to either the clockwise-adjacent subunit (top) or to the counterclockwise-adjacent subunit (bottom) revealing that the new $P2_1$ structures differ from the original P1 model primarily in the position of subunit F, and in the Q and R-loops of subunits A and E.

bioRxiv preprint doi: https://doi.org/10.1101/069559; this version posted August 16, 2016. The copyright holder for this preprint (which was not certified by peer review) is the author/funder. All rights reserved. No reuse allowed without permission.

**Figure 3.** Changes in ADP•$BeF_3$ coordination as revealed by superpositions between six $Rho^{PolyU\text{-}P1}$ (white) and $Rho^{PolyU\text{-}P2_1}$ (colored) ATPase centers. In all subunits, changes are consistent with a partial shift in catalytic status of the six active sites around the ring. Abbreviations: WA – Walker A, WB – Walker B, RS – arginine switch, RF – arginine finger, RV – arginine valve. (**a**) Subunit A/B interface. While a water molecule is observed to associate with the catalytic glutamate (CE) at this site in $Rho^{PolyU\text{-}P1}$ (water 4), it is not observed in the new $Rho^{PolyU\text{-}P2_1}$ structure. (**b**) Subunit B/C interface. Both catalytic centers show bonding interactions (dashed lines) characteristic of the *T* and *T** states. Inset shows a zoomed-in view of the catalytic center with the RV removed (for clarity): whereas the prospective attacking water molecule in $Rho^{PolyU\text{-}P1}$ was not ideally positioned for in-line chemistry with the γ-phosphate moiety (mimicked by the $BeF_3$ – white), the CE-associated water molecules seen in the *T** states of the new $Rho^{PolyU\text{-}P2_1}$ are positioned for ideal in-line attack (red arrow). (**c**) Subunit C/D interface. Concomitant with the disappearance of the catalytic water molecule in the A/B subunit interface of the $Rho^{PolyU\text{-}P2_1}$ structure, a catalytic water molecule appears in the C/D subunit interface compared to the $Rho^{PolyU\text{-}P1}$ structure. (**d**) Subunit D/E interface. This site retains contacts characteristic of the *T* state in both structures. The CE in $Rho^{PolyU\text{-}P2_1}$ has broken its atypical contact with the $Mg^{2+}$ ion observed in $Rho^{PolyU\text{-}P1}$, suggesting that it is transitioning to a slightly more active arrangement. (**e**) Subunit E/F interface. The arginine finger in the $Rho^{PolyU\text{-}P1}$ *E*-state appears to be pointing out of the active site, while the arginine finger in $Rho^{PolyU\text{-}P2_1}$ clearly points into the active site and coordinates the bound $BeF_3$. However, the arginine valve in the $Rho^{PolyU\text{-}P2_1}$ structure is pulled slightly out of the active site, resulting in the same number of contacts between the arginine groups and the $BeF_3$ molecule. The catalytic glutamate in this active site is in an atypical conformation in both structures, interacting with the $Mg^{2+}$ ion directly (P1) or indirectly *via* coordinated waters ($P2_1$). Rotated view – the catalytic glutamate and arginine switch in $Rho^{PolyU\text{-}P2_1}$ are moved out of the catalytic site in the *E*-state when compared to the $Rho^{PolyU\text{-}P1}$ structure. (**f**) Subunit F/A interface. The arginine valve in the $Rho^{PolyU\text{-}P1}$ *D*-state points out of the active site, while the arginine valve in the $Rho^{PolyU\text{-}P2_1}$ structure points into the active site and coordinates the bound $BeF_3$. Rotated view – the arginine valve now points into the active site due to an opening of the intersubunit interface in $Rho^{PolyU\text{-}P2_1}$ relative to $Rho^{PolyU\text{-}P1}$ that relieves a steric clash between the guanidinium group of the arginine and G337 of the adjacent subunit.

bioRxiv preprint doi: https://doi.org/10.1101/069559; this version posted August 16, 2016. The copyright holder for this preprint (which was not certified by peer review) is the author/funder. All rights reserved. No reuse allowed without permission.

**Figure 4.** Opening of the active site in the exchange (*E*) state (subunit E) accompanies nucleotide release. (**a**) Simulated annealing omit map of the *E*-state in Rho$^{PolyU\text{-}P2_1}$ revealing strong density for the bound nucleotide. (**b**) Simulated annealing omit map of the *E*-state in the Rho$^{Empty}$ structure reveals poor density suggesting low nucleotide occupancy and/or order. (**c**) Intersubunit distance vectors calculated independently for each intersubunit interface and comparing Rho$^{Empty}$ and Rho$^{PolyU\text{-}P2_1}$ structures. The vectors reveal that the only significant intersubunit changes between these structures are at the E/F interface. (**d**) Superposition of chain E from the Rho$^{PolyU\text{-}P2_1}$ and Rho$^{Empty}$ structures reveals that nucleotide release induces a rigid body shift in chain F (arrows) that causes the active site to open. The arginine finger (RF), which also changes position, is labeled. (**e**) Structural alignments showing that the E/F suubnit (*E*-state) interface of Rho$^{Empty}$ aligns almost perfectly with an open-ring intersubunit interface (left), as opposed contrast to the B/C subunit (*T**-state) subunit interface of Rho$^{PolyU\text{-}P2_1}$, which has adopted a right-handed orientation (right, red arrows).

**Figure 5.** Comparison of RNA binding among closed-ring Rho structures. The five core RNA bases common to all structures are colored white, while additional 5'- and 3'-bases are colored orange. Arrows at the 5' and 3' end of the bound RNA indicate the direction of RNA translocation relative to the protein. Protein subunits are colored as in **Fig. 2a**. Insets reveal protein-RNA hydrogen bonding details (dashed lines) at the B/C subunit interface. (**a**) Rho$^{PolyU\text{-}P1}$ contains six bases of RNA (orange/white) bound by the Rho Q- and R-loops in a spiral staircase conformation. (**b**) The Rho$^{Empty}$ structure allows for the modeling of eight bases of RNA (orange/white). Compared to the Rho$^{PolyU\text{-}P_1}$ structure, there is additional density for two 3' bases in a kinked conformation. (**c**) The Rho$^{PolyU\text{-}P2_1}$ structure allows for modeling of seven bases of RNA (orange/white). Compared to the Rho$^{Empty}$ structure, density is lacking for the 5' base. This structure reveals a hydrogen bonding network stabilizing interactions between R-loop residue K326 of subunits B and C, a water molecule, and the 2'-OH and uracil base of the bound RNA kink. (**d**) The structure of Rho$^{PolyA}$ solved under similar conditions to Rho$^{PolyU\text{-}P2_1}$, also reveals two additional 3' bases, but in a pseudo A-form helical arrangement, rather than the kinked conformation; in contrast to the H-bonding network observed with the kinked PolyU substrate, no additional protein-RNA contacts are formed.

bioRxiv preprint doi: https://doi.org/10.1101/069559; this version posted August 16, 2016. The copyright holder for this preprint (which was not certified by peer review) is the author/funder. All rights reserved. No reuse allowed without permission.

**Figure 6.** A conserved allosteric helix couples pore loop movement and ATPase status in RecA-like hexameric motors. (**a**) An α-helix (Rα1, cartoon) in each subunit of the Rho hexameric motor domain (transparent surface) directly connects the RNA and ATP binding sites. RNA – orange, nucleotide – magenta, catalytic water molecules – red spheres (subunits B and C only). Lys326 (colored sticks) directly connects the allosteric helix to bound RNA. (**b**) Alignment of all active sites in $Rho^{PolyU\text{-}P2_1}$ reveals the consequences of inter-subunit conformational transitions in the allosteric helix. The helix itself directly links the RNA binding R-loops in the center of the ring to the position of the γ-phosphate sensing residues in the ATP-binding sites at the periphery of the ring, as well as to the catalytic water in the *T** active sites. Dashed lines (colored by interface) show bonding interactions present in the B/C, C/D and D/E subunit interfaces. Abbreviations: RV – arginine valve, RF – arginine finger. (**c**) Alignment of the catalytic site in the C/D subunit interface of $Rho^{PolyU\text{-}P2_1}$ (white) with the catalytic site in the structure of the $F_1$-ATPase bound to ADP•$BeF_3$ (colored, PDB ID: 1W0J) reveals nearly identical alignments of the catalytic residues and the backbone carbonyl groups of the allosteric helix (60). Lower panel – position of the $F_1$ allosteric helix with respect to the rotating γ-subunit shaft. (**d**) The structure of DnaB bound to nucleic acid and GDP•$AlF_4$ reveals interactions between its analog of helix Rα1 and γ-phosphate sensing residues (31). (**e**) The structure of RecA bound to double-stranded DNA and ADP•$AlF_4$ reveals a similar helix configuration as in panels **b-d** (61). KF – lysine finger.

**Figure 7.** Sub-stepping in a hexameric helicase. (*Top, red dashed box*) Diagram of RNA bases and catalytic states in the $Rho^{PolyU\text{-}P1}$, $Rho^{PolyU\text{-}P2_1}$, and $Rho^{Empty}$ structures. Protein subunits are shown as large spheres colored by chain as in **Fig. 2a**. Arrows indicate the sequence of proposed sub-steps in which an incoming 3' RNA base is bound and a 5' RNA base is released consistent release of nucleotide and a shift in position of the *T** catalytic states. Yellow stars designate the sites of the nucleophilic water observed in the various Rho structures; only in the $Rho^{PolyU\text{-}P2_1}$ structure does this water adopt an in-line attack position. (*Bottom*) Relationship of the substeps to a complete series of six sequential hydrolysis and translocation steps by Rho.

bioRxiv preprint doi: https://doi.org/10.1101/069559; this version posted August 16, 2016. The copyright holder for this preprint (which was not certified by peer review) is the author/funder. All rights reserved. No reuse allowed without permission.

## REFERENCES


1. Delagoutte E & von Hippel PH (2003) Helicase mechanisms and the coupling of helicases within macromolecular machines. Part II: Integration of helicases into cellular processes. *Q Rev Biophys* 36(1):1-69.
2. Patel SS & Picha KM (2000) Structure and function of hexameric helicases. *Annu Rev Biochem* 69:651-697.
3. Singleton MR, Dillingham MS, & Wigley DB (2007) Structure and mechanism of helicases and nucleic acid translocases. *Annual review of biochemistry* 76:23-50.
4. Sauer RT & Baker TA (2011) AAA+ proteases: ATP-fueled machines of protein destruction. *Annual review of biochemistry* 80:587-612.
5. Ahnert P, Picha KM, & Patel SS (2000) A ring-opening mechanism for DNA binding in the central channel of the T7 helicase-primase protein. *The EMBO journal* 19(13):3418-3427.
6. O'Shea VL & Berger JM (2014) Loading strategies of ring-shaped nucleic acid translocases and helicases. *Current opinion in structural biology* 25:16-24.
7. Davey MJ, Jeruzalmi D, Kuriyan J, & O'Donnell M (2002) Motors and switches: AAA+ machines within the replisome. *Nature reviews. Molecular cell biology* 3(11):826-835.
8. Richardson JP (2002) Rho-dependent termination and ATPases in transcript termination. *Biochim Biophys Acta* 1577(2):251-260.
9. Boudvillain M, Nollmann M, & Margeat E (2010) Keeping up to speed with the transcription termination factor Rho motor. *Transcr* 1(2):70-75.
10. Dombroski AJ & Platt T (1988) Structure of rho factor: an RNA-binding domain and a separate region with strong similarity to proven ATP-binding domains. *Proc Natl Acad Sci U S A* 85(8):2538-2542.
11. Bear DG*, et al.* (1985) Escherichia coli transcription termination factor rho has a two-domain structure in its activated form. *Proceedings of the National Academy of Sciences of the United States of America* 82(7):1911-1915.
12. Chen CY & Richardson JP (1987) Sequence elements essential for rho-dependent transcription termination at lambda tR1. *J Biol Chem* 262(23):11292-11299.
13. Peters JM*, et al.* (2012) Rho and NusG suppress pervasive antisense transcription in Escherichia coli. *Genes & development* 26(23):2621-2633.
14. Epshtein V, Dutta D, Wade J, & Nudler E (2010) An allosteric mechanism of Rho-dependent transcription termination. *Nature* 463(7278):245-249.
15. Brennan CA, Dombroski AJ, & Platt T (1987) Transcription termination factor rho is an RNA-DNA helicase. *Cell* 48(6):945-952.
16. Park JS & Roberts JW (2006) Role of DNA bubble rewinding in enzymatic transcription termination. *Proceedings of the National Academy of Sciences of the United States of America* 103(13):4870-4875.
17. Lau LF, Roberts JW, & Wu R (1983) RNA polymerase pausing and transcript release at the lambda tR1 terminator in vitro. *J Biol Chem* 258(15):9391-9397.
18. Morgan WD, Bear DG, & von Hippel PH (1983) Rho-dependent termination of transcription. II. Kinetics of mRNA elongation during transcription from the bacteriophage lambda PR promoter. *J Biol Chem* 258(15):9565-9574.
19. Koslover DJ, Fazal FM, Mooney RA, Landick R, & Block SM (2012) Binding and translocation of termination factor rho studied at the single-molecule level. *Journal of molecular biology* 423(5):664-676.

bioRxiv preprint doi: https://doi.org/10.1101/069559; this version posted August 16, 2016. The copyright holder for this preprint (which was not certified by peer review) is the author/funder. All rights reserved. No reuse allowed without permission.

20. Gogol EP, Seifried SE, & von Hippel PH (1991) Structure and assembly of the Escherichia coli transcription termination factor rho and its interaction with RNA. I. Cryoelectron microscopic studies. *Journal of molecular biology* 221(4):1127-1138.
21. Bear DG*, et al.* (1988) Interactions of Escherichia coli transcription termination factor rho with RNA. II. Electron microscopy and nuclease protection experiments. *Journal of molecular biology* 199(4):623-635.
22. Skordalakes E & Berger JM (2003) Structure of the Rho transcription terminator: mechanism of mRNA recognition and helicase loading. *Cell* 114(1):135-146.
23. Skordalakes E & Berger JM (2006) Structural insights into RNA-dependent ring closure and ATPase activation by the Rho termination factor. *Cell* 127(3):553-564.
24. Yu X, Horiguchi T, Shigesada K, & Egelman EH (2000) Three-dimensional reconstruction of transcription termination factor rho: orientation of the N-terminal domain and visualization of an RNA-binding site. *J Mol Biol* 299(5):1279-1287.
25. Richardson JP (2003) Loading Rho to terminate transcription. *Cell* 114(2):157-159.
26. Costa A*, et al.* (2011) The structural basis for MCM2-7 helicase activation by GINS and Cdc45. *Nature structural & molecular biology* 18(4):471-477.
27. Lyubimov AY, Costa A, Bleichert F, Botchan MR, & Berger JM (2012) ATP-dependent conformational dynamics underlie the functional asymmetry of the replicative helicase from a minimalist eukaryote. *Proceedings of the National Academy of Sciences of the United States of America* 109(30):11999-12004.
28. Bochman ML & Schwacha A (2010) The Saccharomyces cerevisiae Mcm6/2 and Mcm5/3 ATPase active sites contribute to the function of the putative Mcm2-7 'gate'. *Nucleic Acids Res* 38(18):6078-6088.
29. Thomsen ND & Berger JM (2009) Running in reverse: the structural basis for translocation polarity in hexameric helicases. *Cell* 139(3):523-534.
30. Enemark EJ & Joshua-Tor L (2006) Mechanism of DNA translocation in a replicative hexameric helicase. *Nature* 442(7100):270-275.
31. Itsathitphaisarn O, Wing RA, Eliason WK, Wang J, & Steitz TA (2012) The Hexameric Helicase DnaB Adopts a Nonplanar Conformation during Translocation. *Cell*.
32. Singleton MR, Sawaya MR, Ellenberger T, & Wigley DB (2000) Crystal structure of T7 gene 4 ring helicase indicates a mechanism for sequential hydrolysis of nucleotides. *Cell* 101(6):589-600.
33. Abrahams JP, Leslie AG, Lutter R, & Walker JE (1994) Structure at 2.8 A resolution of F1-ATPase from bovine heart mitochondria. *Nature* 370(6491):621-628.
34. Costa A*, et al.* (2014) DNA binding polarity, dimerization, and ATPase ring remodeling in the CMG helicase of the eukaryotic replisome. *eLife* 3:e03273.
35. Rothenberg E, Trakselis MA, Bell SD, & Ha T (2007) MCM forked substrate specificity involves dynamic interaction with the 5'-tail. *The Journal of biological chemistry* 282(47):34229-34234.
36. Schwartz A*, et al.* (2009) A stepwise 2'-hydroxyl activation mechanism for the bacterial transcription termination factor Rho helicase. *Nat Struct Mol Biol* 16(12):1309-1316.
37. Wang Y & von Hippel PH (1993) Escherichia coli transcription termination factor rho. I. ATPase activation by oligonucleotide cofactors. *The Journal of biological chemistry* 268(19):13940-13946.

bioRxiv preprint doi: https://doi.org/10.1101/069559; this version posted August 16, 2016. The copyright holder for this preprint (which was not certified by peer review) is the author/funder. All rights reserved. No reuse allowed without permission.

38. Richardson JP (1982) Activation of rho protein ATPase requires simultaneous interaction at two kinds of nucleic acid-binding sites. *The Journal of biological chemistry* 257(10):5760-5766.
39. Soares E, Schwartz A, Nollmann M, Margeat E, & Boudvillain M (2014) The RNA-mediated, asymmetric ring regulatory mechanism of the transcription termination Rho helicase decrypted by time-resolved nucleotide analog interference probing (trNAIP). *Nucleic acids research* 42(14):9270-9284.
40. Putnam CD, Hammel M, Hura GL, & Tainer JA (2007) X-ray solution scattering (SAXS) combined with crystallography and computation: defining accurate macromolecular structures, conformations and assemblies in solution. *Quarterly reviews of biophysics* 40(3):191-285.
41. Konarev PV, Volkov VV, Sokolova AV, Koch MHJ, & Svergun DI (2003) PRIMUS: a Windows PC-based system for small-angle scattering data analysis. *J Appl Crystallogr* 36:1277-1282.
42. Schneidman-Duhovny D, Hammel M, Tainer JA, & Sali A (2013) Accurate SAXS profile computation and its assessment by contrast variation experiments. *Biophysical journal* 105(4):962-974.
43. Schneidman-Duhovny D, Hammel M, & Sali A (2010) FoXS: a web server for rapid computation and fitting of SAXS profiles. *Nucleic acids research* 38(Web Server issue):W540-544.
44. Jeong YJ, Kim DE, & Patel SS (2004) Nucleotide binding induces conformational changes in Escherichia coli transcription termination factor Rho. *The Journal of biological chemistry* 279(18):18370-18376.
45. Lawson MR, Dyer K, & Berger JM Ligand-induced and small molecule control of substrate loading in a hexameric helicase.
46. Thomsen ND & Berger JM (2012) Crystallization and X-ray structure determination of an RNA-dependent hexameric helicase. *Methods in enzymology* 511:171-190.
47. Frauenfelder H, Petsko GA, & Tsernoglou D (1979) Temperature-dependent X-ray diffraction as a probe of protein structural dynamics. *Nature* 280(5723):558-563.
48. Geiselmann J & von Hippel PH (1992) Functional interactions of ligand cofactors with Escherichia coli transcription termination factor rho. I. Binding of ATP. *Protein Sci* 1(7):850-860.
49. Kim DE & Patel SS (1999) The mechanism of ATP hydrolysis at the noncatalytic sites of the transcription termination factor Rho. *J Biol Chem* 274(46):32667-32671.
50. Kim DE, Shigesada K, & Patel SS (1999) Transcription termination factor Rho contains three noncatalytic nucleotide binding sites. *J Biol Chem* 274(17):11623-11628.
51. Seifried SE, Easton JB, & von Hippel PH (1992) ATPase activity of transcription-termination factor rho: functional dimer model. *Proc Natl Acad Sci U S A* 89(21):10454-10458.
52. Stitt BL (1988) Escherichia coli transcription termination protein rho has three hydrolytic sites for ATP. *J Biol Chem* 263(23):11130-11137.
53. Xu Y, Johnson J, Kohn H, & Widger WR (2003) ATP binding to Rho transcription termination factor. Mutant F355W ATP-induced fluorescence quenching reveals dynamic ATP binding. *The Journal of biological chemistry* 278(16):13719-13727.
54. Rabhi M*, et al.* (2011) Mutagenesis-based evidence for an asymmetric configuration of the ring-shaped transcription termination factor Rho. *J Mol Biol* 405(2):497-518.

bioRxiv preprint doi: https://doi.org/10.1101/069559; this version posted August 16, 2016. The copyright holder for this preprint (which was not certified by peer review) is the author/funder. All rights reserved. No reuse allowed without permission.


55. Miwa Y, Horiguchi T, & Shigesada K (1995) Structural and functional dissections of transcription termination factor rho by random mutagenesis. *J Mol Biol* 254(5):815-837.
56. Wei RR & Richardson JP (2001) Identification of an RNA-binding Site in the ATP binding domain of Escherichia coli Rho by H2O2/Fe-EDTA cleavage protection studies. *J Biol Chem* 276(30):28380-28387.
57. Xu Y, Kohn H, & Widger WR (2002) Mutations in the rho transcription termination factor that affect RNA tracking. *The Journal of biological chemistry* 277(33):30023-30030.
58. Balasubramanian K & Stitt BL (2010) Evidence for amino acid roles in the chemistry of ATP hydrolysis in Escherichia coli Rho. *Journal of molecular biology* 404(4):587-599.
59. Lowery-Goldhammer C & Richardson JP (1974) An RNA-dependent nucleoside triphosphate phosphohydrolase (ATPase) associated with rho termination factor. *Proc Natl Acad Sci U S A* 71(5):2003-2007.
60. Kagawa R, Montgomery MG, Braig K, Leslie AG, & Walker JE (2004) The structure of bovine F1-ATPase inhibited by ADP and beryllium fluoride. *EMBO J* 23(14):2734-2744.
61. Chen Z, Yang H, & Pavletich NP (2008) Mechanism of homologous recombination from the RecA-ssDNA/dsDNA structures. *Nature* 453(7194):489-484.
62. Lowry OH, Carter J, Ward JB, & Glaser L (1971) The effect of carbon and nitrogen sources on the level of metabolic intermediates in Escherichia coli. *J Biol Chem* 246(21):6511-6521.
63. Bennett BD*, et al.* (2009) Absolute metabolite concentrations and implied enzyme active site occupancy in Escherichia coli. *Nat Chem Biol* 5(8):593-599.
64. Albe KR, Butler MH, & Wright BE (1990) Cellular concentrations of enzymes and their substrates. *J Theor Biol* 143(2):163-195.
65. Bailey S, Eliason WK, & Steitz TA (2007) Structure of hexameric DnaB helicase and its complex with a domain of DnaG primase. *Science (New York, N.Y.)* 318(5849):459-463.
66. Sanders CM*, et al.* (2007) Papillomavirus E1 helicase assembly maintains an asymmetric state in the absence of DNA and nucleotide cofactors. *Nucleic acids research* 35(19):6451-6457.
67. Johnson DS, Bai L, Smith BY, Patel SS, & Wang MD (2007) Single-molecule studies reveal dynamics of DNA unwinding by the ring-shaped T7 helicase. *Cell* 129(7):1299-1309.
68. Patel SS (2009) Structural biology: Steps in the right direction. *Nature* 462(7273):581-583.
69. Liao J-C, Jeong Y-J, Kim D-E, Patel SS, & Oster G (2005) Mechanochemistry of T7 DNA Helicase. *Journal of Molecular Biology* 350(3):452-475.
70. Kull FJ, Sablin EP, Lau R, Fletterick RJ, & Vale RD (1996) Crystal structure of the kinesin motor domain reveals a structural similarity to myosin. *Nature* 380(6574):550-555.
71. Sablin EP*, et al.* (1998) Direction determination in the minus-end-directed kinesin motor ncd. *Nature* 395(6704):813-816.
72. Schmidt H, Zalyte R, Urnavicius L, & Carter AP (2014) Structure of human cytoplasmic dynein-2 primed for its power stroke. *Nature*.
73. Rees DM, Montgomery MG, Leslie AG, & Walker JE (2012) Structural evidence of a new catalytic intermediate in the pathway of ATP hydrolysis by F1-ATPase from bovine

bioRxiv preprint doi: https://doi.org/10.1101/069559; this version posted August 16, 2016. The copyright holder for this preprint (which was not certified by peer review) is the author/funder. All rights reserved. No reuse allowed without permission.

heart mitochondria. *Proceedings of the National Academy of Sciences of the United States of America* 109(28):11139-11143.

74. Chistol G*, et al.* (2012) High degree of coordination and division of labor among subunits in a homomeric ring ATPase. *Cell* 151(5):1017-1028.
75. Yasuda R, Noji H, Yoshida M, Kinosita K, Jr., & Itoh H (2001) Resolution of distinct rotational substeps by submillisecond kinetic analysis of F1-ATPase. *Nature* 410(6831):898-904.
76. Konarev PV, Volkov VV, Sokolova AV, Koch MHJ, & Svergun DI (2003) PRIMUS: a Windows PC-based system for small-angle scattering data analysis. *Journal of Applied Crystallography* 36(5):1277-1282.
77. Petoukhov MV, Konarev PV, Kikhney AG, & Svergun DI (2007) ATSAS 2.1 - towards automated and web-supported small-angle scattering data analysis. *J Appl Cryst* 40:s223-s228.
78. Svergun DI (1992) Determination of the regularization parameter in indirect-transform methods using perceptual criteria. *J Appl Crystallogr* 25:495-503.
79. Svergun D, Barberato C, & Koch MHJ (1995) CRYSOL - a Program to Evaluate X-ray Solution Scattering of Biological Macromolecules from Atomic Coordinates. *Journal of Applied Crystallography* 28(6):768-773.
80. MacDowell AA*, et al.* (2004) Suite of three protein crystallography beamlines with single superconducting bend magnet as the source. *J Synchrotron Radiat* 11(Pt 6):447-455.
81. Otwinowski Z & Minor W (1997) Processing of X-ray Diffraction Data Collected in Oscillation Mode. *Methods in Enzymology*, eds Carter CW, Jr. & Sweet RM (Academic Press, New York), Vol 276: Macromolecular Crysallography, part A, pp 307-326.
82. Adams PD*, et al.* (2010) PHENIX: a comprehensive Python-based system for macromolecular structure solution. *Acta Crystallogr D Biol Crystallogr* 66(Pt 2):213-221.
83. McCoy AJ*, et al.* (2007) Phaser crystallographic software. *Journal of Applied Crystallography* 40(4):658-674.
84. Terwilliger TC (2000) Maximum-likelihood density modification. *Acta Crystallogr D Biol Crystallogr* 56(Pt 8):965-972.
85. Davis IW*, et al.* (2007) MolProbity: all-atom contacts and structure validation for proteins and nucleic acids. *Nucleic Acids Res* 35(Web Server issue):W375-383.
86. Painter J & Merritt EA (2006) TLSMD web server for the gernation of multi-group TLS models. *J Appl Cryst* 39:109-111.
87. Shindyalov IN & Bourne PE (1998) Protein structure alignment by incremental combinatorial extension (CE) of the optimal path. *Protein Eng* 11(9):739-747.
88. Flores S*, et al.* (2006) The Database of Macromolecular Motions: new features added at the decade mark. *Nucleic Acids Res* 34(Database issue):D296-301.
89. Zhang W, Dunkle JA, & Cate JH (2009) Structures of the ribosome in intermediate states of ratcheting. *Science* 325(5943):1014-1017.

Figure 1

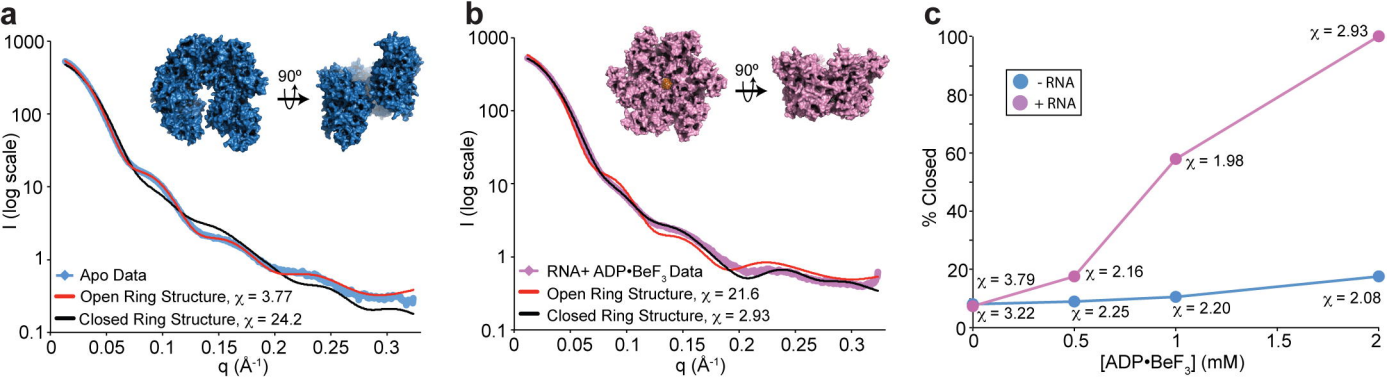
a
1000
100
10
1
0.1
I (log scale)
90º
Apo Data
Open Ring Structure, χ = 3.77
Closed Ring Structure, χ = 24.2
0
0.05
0.1
0.15
0.2
0.25
0.3
q (Å-1)
b
RNA+ ADP•BeF3 Data
Open Ring Structure, χ = 21.6
Closed Ring Structure, χ = 2.93
c
100
80
60
40
20
0
% Closed
- RNA
+ RNA
χ = 2.93
χ = 1.98
χ = 3.79
χ = 2.16
χ = 3.22
χ = 2.25
χ = 2.20
χ = 2.08
0
0.5
1
1.5
2
[ADP•BeF3] (mM)

Figure 2

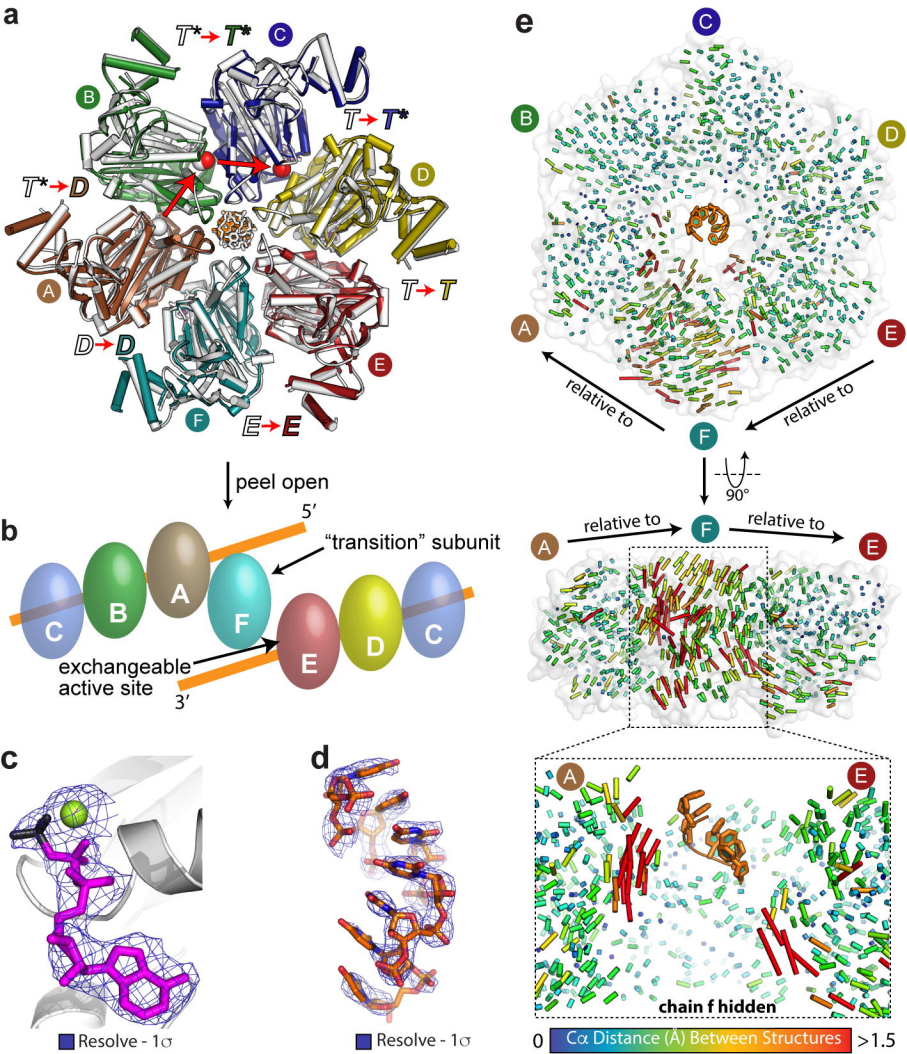
a
T*→T*
T→T*
T*→D
T→T
D→D
E→E
peel open
5′
3′
"transition" subunit
exchangeable
active site
b
c
d
Resolve - 1σ
Resolve - 1σ
e
relative to
relative to
90°
relative to
relative to
chain f hidden
0
Cα Distance (Å) Between Structures
>1.5

Figure 3

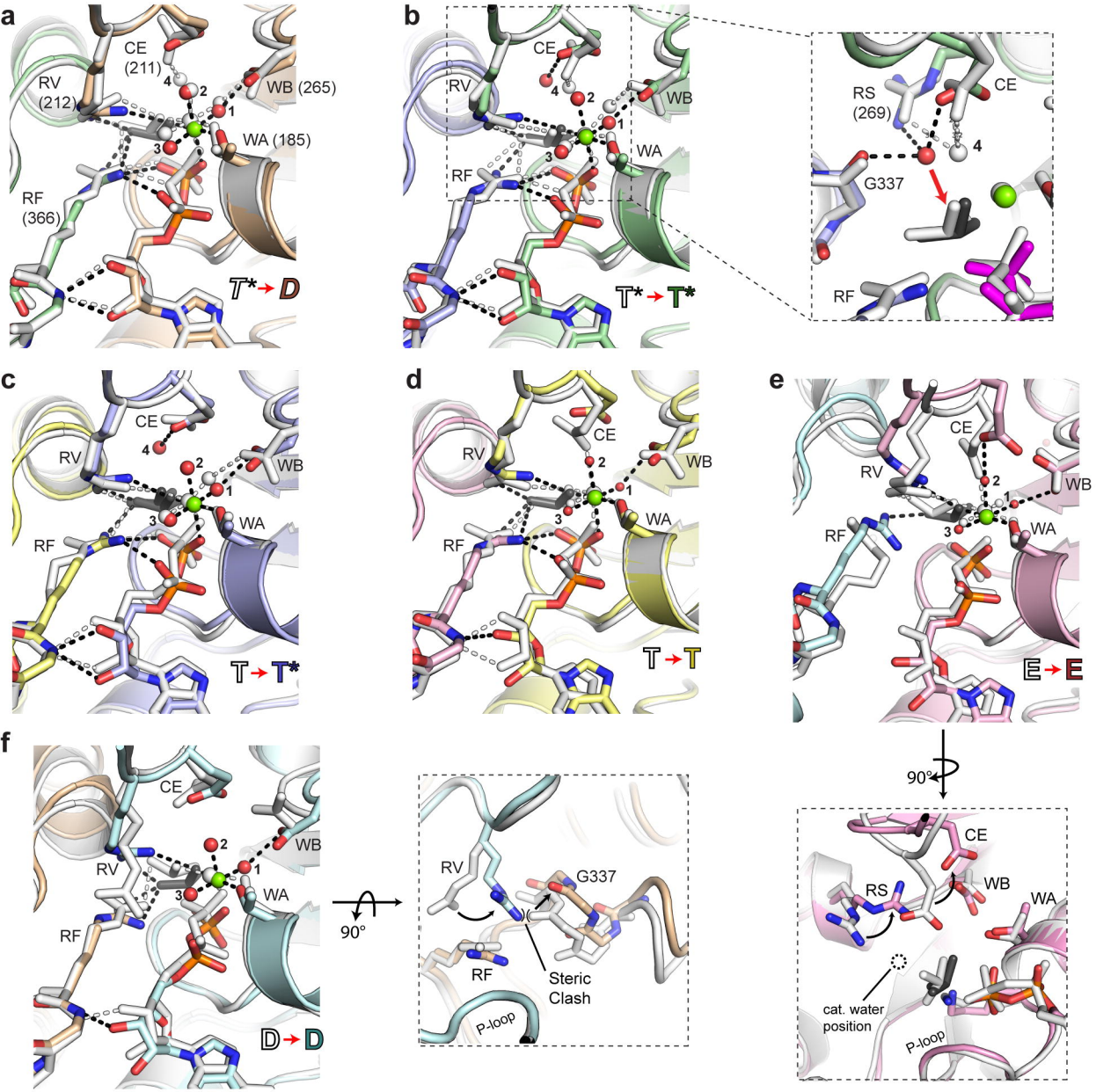
a
CE
(211)
RV
(212)
WB (265)
WA (185)
RF
(366)
T*→D
b
CE
RV
WB
WA
RF
T*→T*
RS
(269)
CE
G337
RF
c
CE
RV
WB
WA
RF
T→T*
d
CE
RV
WB
WA
RF
T→T
e
CE
RV
WB
WA
RF
E→E
90°
CE
RS
WB
WA
cat. water
position
P-loop
f
CE
RV
WB
WA
RF
D→D
90°
RV
G337
RF
Steric
Clash
P-loop
Key:
A
B
C
D
E
F

Figure 4

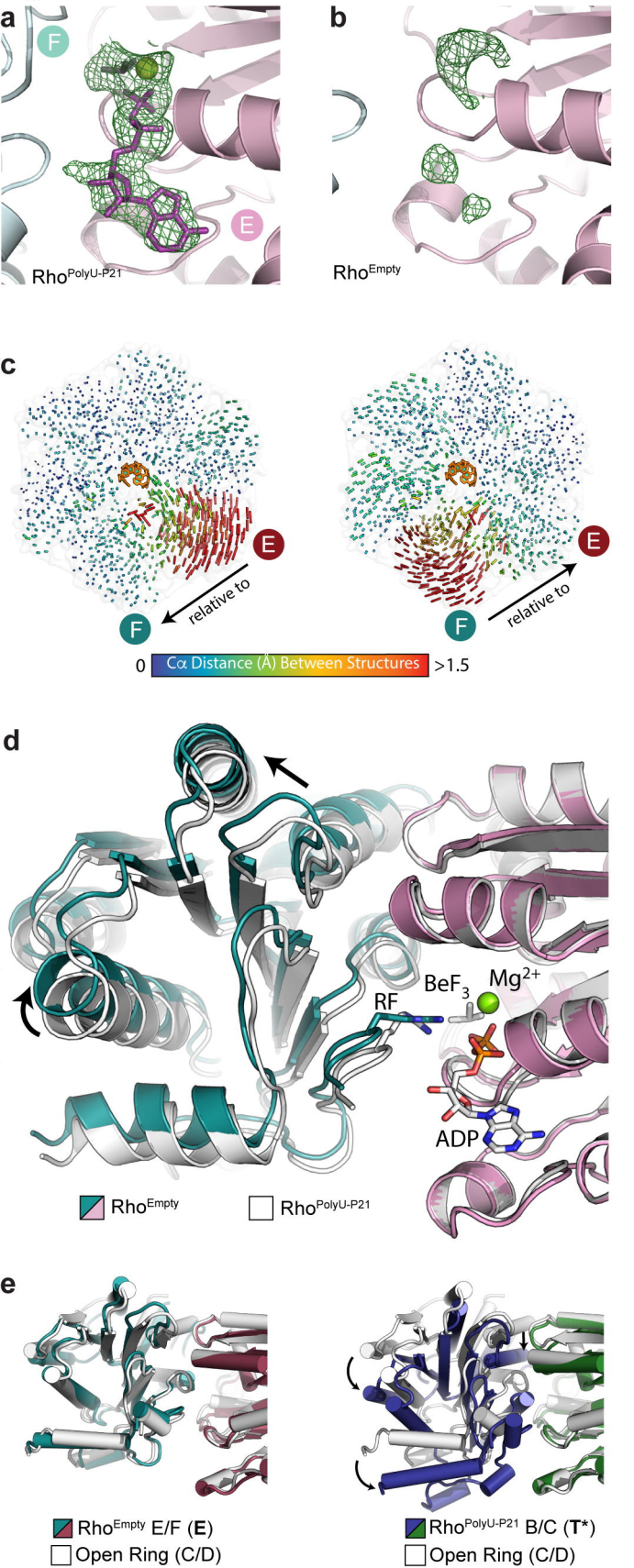
a
F
E
Rho^PolyU-P21
b
Rho^Empty
c
E
relative to
F
E
relative to
F
0
Cα Distance (Å) Between Structures
>1.5
d
RF
BeF3
Mg2+
ADP
Rho^Empty
Rho^PolyU-P21
e
Rho^Empty E/F (E)
Open Ring (C/D)
Rho^PolyU-P21 B/C (T*)
Open Ring (C/D)

Figure 5

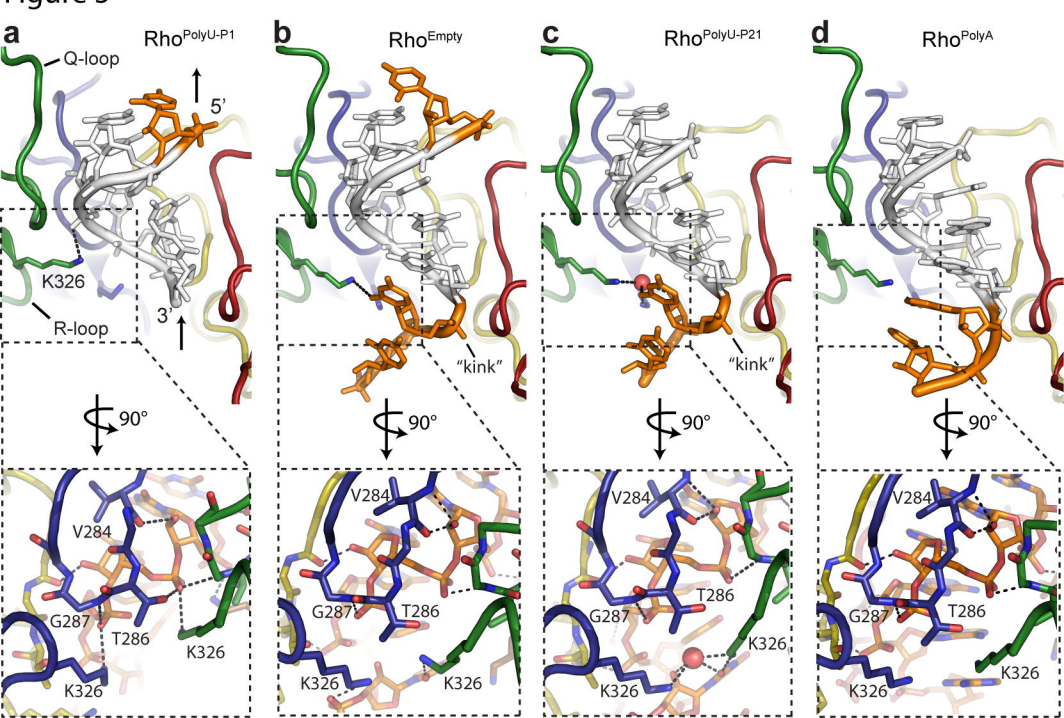
a
Rho^PolyU-P1
Q-loop
5'
3'
K326
R-loop
90°
V284
G287
T286
K326
K326
b
Rho^Empty
"kink"
90°
V284
G287
T286
K326
K326
c
Rho^PolyU-P21
"kink"
90°
V284
T286
G287
K326
K326
d
Rho^PolyA
90°
V284
T286
G287
K326
K326

Figure 6

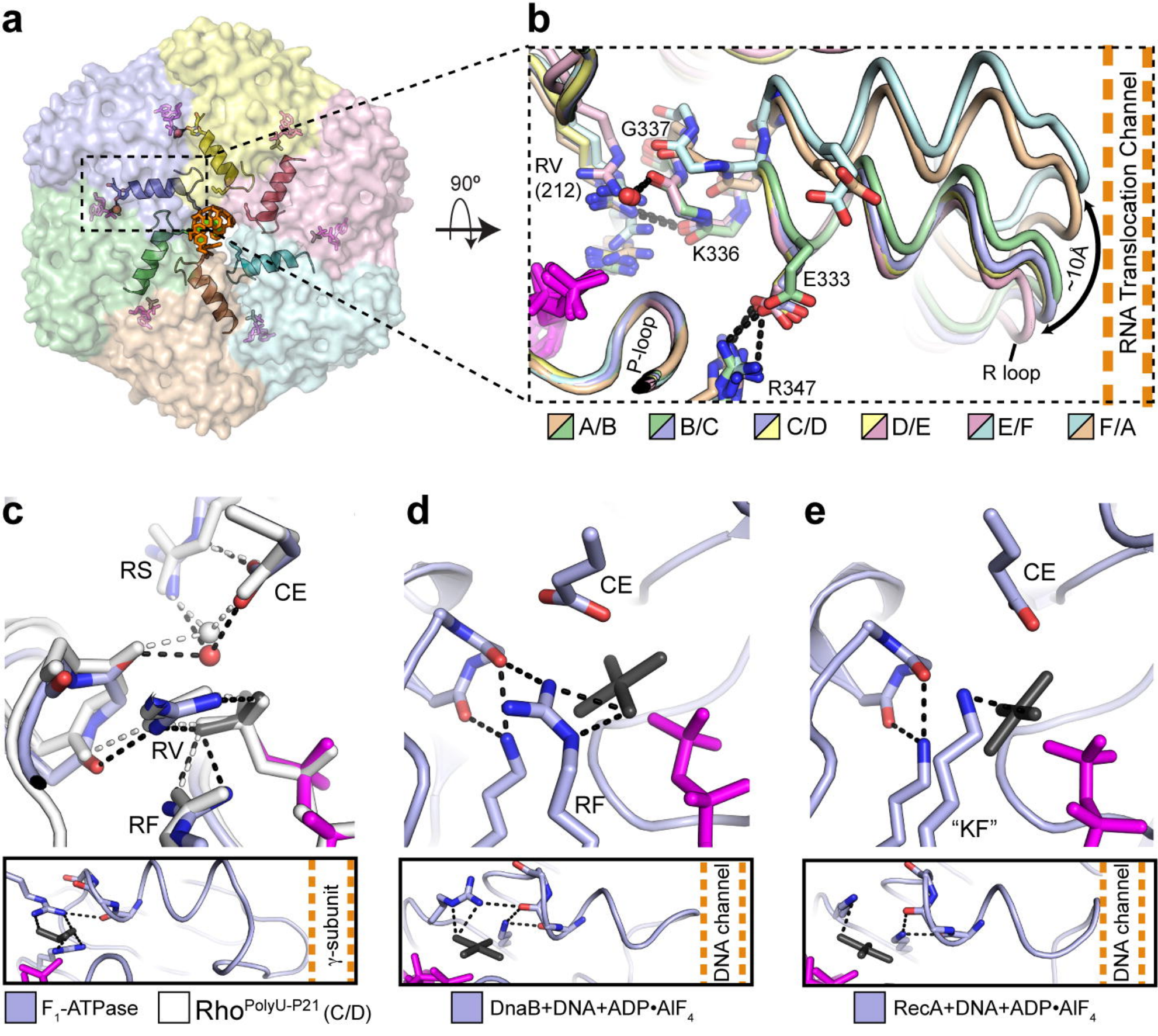
a
b
90°
G337
RV
(212)
K336
E333
P-loop
R347
R loop
~10Å
RNA Translocation Channel
A/B
B/C
C/D
D/E
E/F
F/A
c
RS
CE
RV
RF
γ-subunit
d
CE
RF
DNA channel
e
CE
"KF"
DNA channel
F1-ATPase
RhoPolyU-P21 (C/D)
DnaB+DNA+ADP•AlF4
RecA+DNA+ADP•AlF4

Figure 7

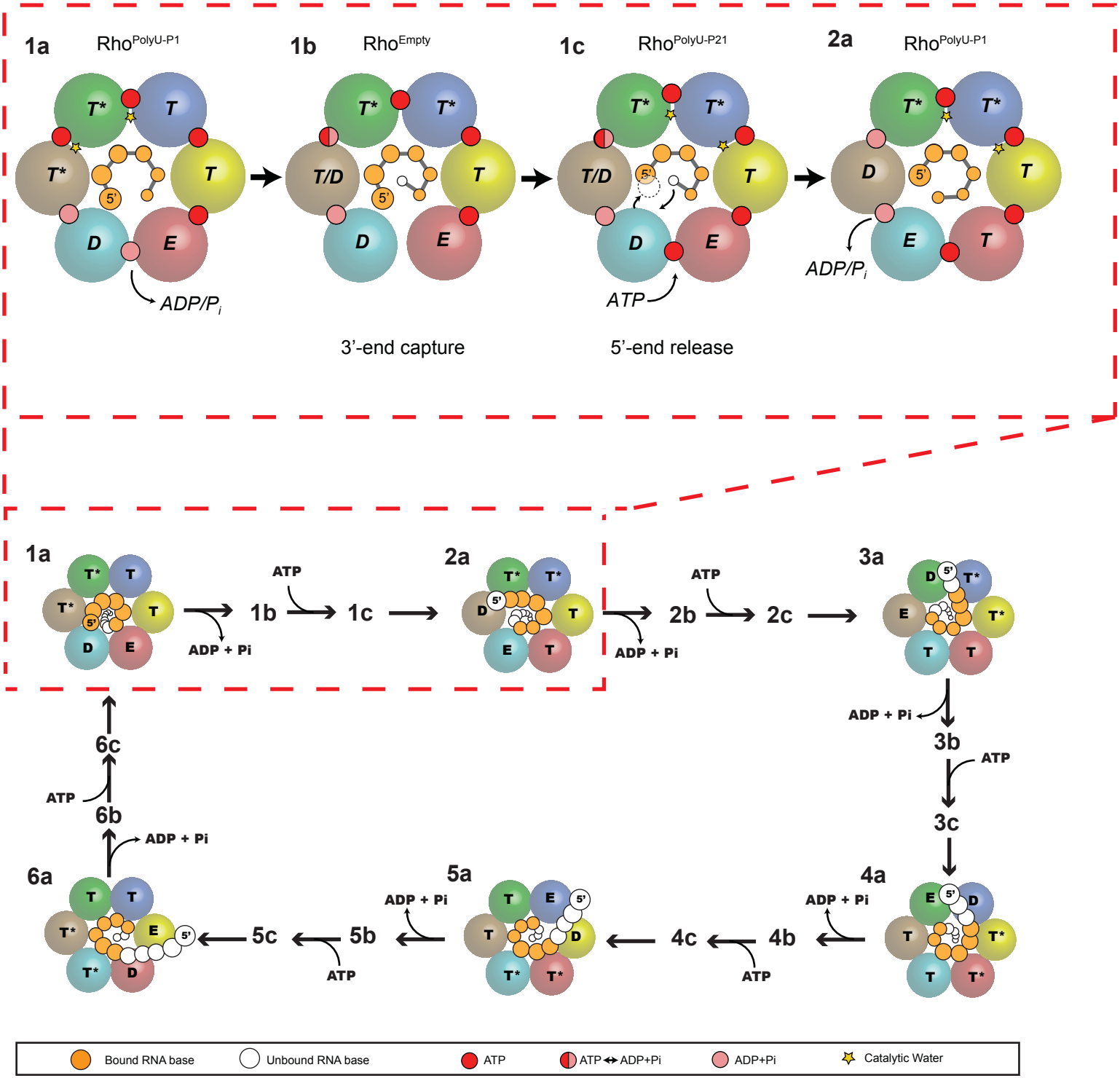
1a
Rho PolyU-P1
1b
Rho Empty
1c
Rho PolyU-P21
2a
Rho PolyU-P1
ADP/Pi
3'-end capture
5'-end release
ATP
ADP/Pi
1a
1b
1c
2a
2b
2c
3a
3b
3c
4a
4b
4c
5a
5b
5c
6a
6b
6c
ATP
ADP + Pi
Bound RNA base
Unbound RNA base
ATP
ATP ↔ ADP+Pi
ADP+Pi
Catalytic Water